

Electron-Transfer Dynamics from Ru Polypyridyl Complexes to In₂O₃ Nanocrystalline Thin Films

Jianchang Guo, David Stockwell, Xin Ai,[†] Chunxing She, Neil A. Anderson,[‡] and Tianquan Lian*

Department of Chemistry, Emory University, Atlanta, Georgia 30322

Received: November 8, 2005; In Final Form: December 28, 2005

Photoinduced electron injection dynamics from Ru(dcbpy)₂(X)₂ (dcbpy = 4,4'-dicarboxy-2,2'-bipyridine; X₂ = 2SCN[−], 2CN[−], and dcbpy; referenced as RuN3, Ru505, and Ru470) to In₂O₃ nanocrystalline thin films were studied using ultrafast transient IR absorption spectroscopy. After 532 nm excitation of the adsorbates, the dynamics of electron injection from their excited states to In₂O₃ were studied by monitoring the IR absorption of the injected electrons in the semiconductor. The injection kinetics were non-single-exponential. For samples exposed to air, the half rise times, defined as the time of 50% injection yield, were 5 ± 0.8, 85 ± 20, and >200 ps for RuN3, Ru505, and Ru470, respectively. For samples in pH 2 buffer, the corresponding half time for injection from these complexes became 6 ± 1, 105 ± 20, and 18 ± 5 ps. The injection kinetics from RuN3 to In₂O₃ was found to be similar to that to SnO₂. These kinetics traces showed a negligible <100 fs injection component and were very different from those to TiO₂. The dependences of the injection kinetics on adsorbate energetics and the nature of the semiconductors are discussed.

Introduction

Interfacial electron-transfer (ET) dynamics between molecular adsorbates and wide band-gap semiconductor nanoparticles have been a subject of intense research interest in recent years.^{1–7} In addition to its fundamental importance,^{1,8,9} these studies were also motivated by the desire to improve the efficiency of dye-sensitized solar cells (DSSCs).^{4,10–12} Among many possible combinations of dyes and semiconductors, the best conversion efficiency was achieved in solar cells based on Ru(dcbpy)₂-(NCS)₂ (dcbpy = 2,2'-bipyridine-4,4'-biscarboxylate) (called RuN3) sensitized TiO₂ nanocrystalline thin films.^{10–12} High conversion efficiency in DSSCs is in part attributed to an ultrafast charge injection from the sensitizer excited state to the semiconductor^{13–27} and a much slower charge recombination.^{28–32} Much lower conversion efficiencies were reported for solar cells based on other semiconductors, such as ZnO,^{33–35} Nb₂O₅,^{33,34,36–40} SnO₂,^{33,41,42} WO₃,³⁴ Ta₂O₅,³⁴ and In₂O₃.^{33,34} The reasons for their low conversion efficiencies remain unclear. A comparison of electron injection and recombination kinetics in these systems may provide some insights into possible ways to improve their efficiencies and the dependence of ET dynamics on material properties.

Many earlier studies of electron injection dynamics were focused on RuN3 sensitized TiO₂.^{13–27} The injection dynamics in this system were found to be biphasic, consisting of a distinctly <100 fs ultrafast component and slower components on the picosecond or longer time scales. The fast component was shown to result from ultrafast injection from unthermalized excited states, which competed effectively with ultrafast internal and intersystem conversion in the excited-state manifold. The

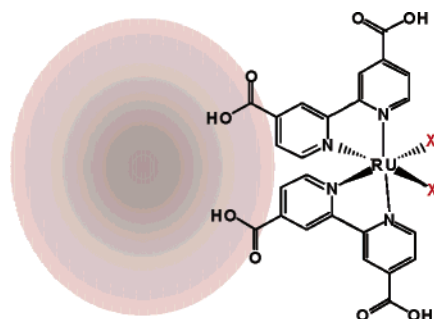
slow component was assigned to injection from the relaxed triplet excited state near the conduction band edge, and the slower rate was attributed to both the reduced density of electron accepting states at the band edge¹⁷ and the intraligand charge-transfer dynamics.²¹ Unlike TiO₂, electron injection dynamics to other semiconductors remain poorly characterized. In an effort to understand its dependence on the properties of semiconductors, we have recently compared electron injection dynamics from Ru polypyridyl dyes to TiO₂,^{6,17} ZnO,^{43,44} Nb₂O₅,⁴⁵ and SnO₂.⁴⁶ At 400 nm excitation, the injection dynamics to these semiconductors were biphasic. However, the amplitude of the fast component and the rate of the slow components are dramatically different. The amplitude of the fast component was found to follow this order: TiO₂ > Nb₂O₅ ≫ SnO₂ ≈ ZnO.^{45,46} Since the fast component amplitude reflects the rate of injection from unthermalized excited states, this trend suggests faster rates to TiO₂ and Nb₂O₅ than to SnO₂ and ZnO. Energetically, the conduction band edges (*E*_{CB}) are similar in TiO₂ and ZnO, while it is ~0.2 eV higher in Nb₂O₅ and ~0.5 eV lower in SnO₂.^{3,47} Therefore, the energetic difference alone is unable to account for the orders of magnitude difference in injection rate to these semiconductors. Instead, we speculated that the difference arose from their conduction band electronic structures. The TiO₂ and Nb₂O₅ conduction bands are comprised primarily of d orbitals of Ti⁴⁺ and Nb⁵⁺, while those of ZnO and SnO₂ being comprised of s and p orbitals of Zn²⁺ and Sn⁴⁺. The d bands are typically narrower and have density of states that are orders of magnitudes higher than those of sp bands.⁴⁷ Furthermore, in TiO₂, the Ti⁴⁺ d orbitals split into T_{2g} and E_g orbitals; the former forms the lower part of the conduction band, and its π symmetry may also allow a stronger electronic coupling with the electron-donating π* orbitals of the bipyridyl ligands in Ru dyes.⁴⁸ Therefore, we have hypothesized that the injection rate of Ru dyes to semiconductors with d-type orbitals in the conduction band is faster than those semiconductors with sp-type orbitals.

To further test the above hypothesis, we investigated the

* Author to whom correspondence should be addressed. E-mail: tlian@emory.edu.

[†] Present address: National Renewable Energy Laboratory, Golden, CO 80401.

[‡] Present address: National Institute of Standards and Technology, Gaithersburg, MD 20899.

CHART 1: Ru(dcbpy)₂(X)₂ Sensitized In₂O₃ Nanoparticles.^a

^a X₂ = 2SCN⁻, 2CN⁻, and dcbpy, referred to as RuN3, Ru505, and Ru470, respectively, dcbpy = 2,2'-bipyridine-4,4'-biscarboxylic acid.

electron injection dynamics of Ru polypyridyl complexes (Chart 1) on In₂O₃ nanocrystalline thin film. The conduction band of In₂O₃ has a band edge position similar to SnO₂,^{3,49} and states near the band edge are composed of empty s orbitals of In³⁺.⁴⁷ Similar band edge position and electronic composition allow an interesting comparison between injection dynamics to In₂O₃ and SnO₂. We find that the injection rates for RuN3 to In₂O₃ and SnO₂ are similar for both films exposed to air and submerged in pH 2 buffer. Unlike those of TiO₂, these injection kinetics traces show negligible <100 fs injection components. Possible origins of these similarities and differences will be discussed.

Experimental Section

Sample Preparations. In₂O₃ nanoparticle colloids were synthesized according to a published procedure.^{50,51} Briefly, 1 g (~3.4 mmol) of InCl₃·4H₂O (97%, from Aldrich) was dissolved in 14 mL of H₂O (Millipore, 18.3 MΩ/cm) in an ice bath under vigorous stirring. After the solution was stirred for 30 min, aqueous ammonia (25%) was added to adjust the pH to ~8, which led to the precipitation of indium hydroxide. The resulting precipitation was centrifuged and dried in a vacuum for 10 min. The precipitation was mixed with 4 mL of H₂O, 1 drop of 2,4-pentanedione (99%, from Aldrich), and 10 drops of TritonX-100 (from Aldrich) and stirred for 2–3 days. The mixture was spread onto sapphire windows by doctor-blade and fired in an oven at 400 °C for 1 h, producing In₂O₃ thin films.

High-purity Ru(dcbpy)₂(X)₂ (X₂ = 2SCN⁻, 2CN⁻, and dcbpy; referred to as RuN3, Ru505, and Ru470, respectively) compounds were purchased from Solaronix (Lausanne, Switzerland). The In₂O₃ films were sensitized by submerging in ethanol solutions of Ru complexes for over 12 h. The sensitized films were then removed from the dye solutions, washed with ethanol, and dried in the air prior to transient absorption measurement. Both sensitized films exposed to air (referred to as dry film) and submerged in pH 2 buffer (pH 2 film) were studied. For the latter samples, sensitized films were submerged in a pH 2 buffer for at least 2 h before transient absorption measurements.

The powder X-ray diffraction (XRD) pattern of In₂O₃ nanocrystals was collected using Bruker D8 diffractometer (equipped with a SMART APEX charge coupled device (CCD) detector). Scanning electron microscopy (SEM) images were collected with a JEOL JSM-7400F FESEM operated at 5 kV. To prepare SEM samples, the In₂O₃ colloid was spread onto silicon chips by doctor-blade and fired in an oven at 400 °C for 1 h before SEM measurement.

Ultrafast Infrared Transient Absorption Measurements.

Ultrafast experiments were carried out in a pump–probe

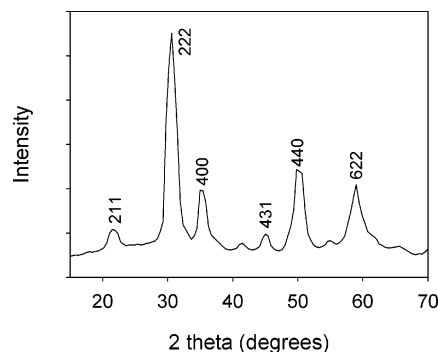


Figure 1. XRD pattern of In₂O₃ nanoparticles.

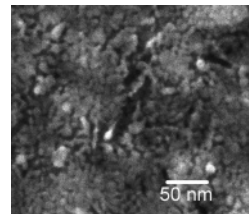


Figure 2. Scanning electron microscopy image of an In₂O₃ nanocrystalline thin film.

transient absorption spectrometer, and the details of the setup have been reported previously.^{17,45,46,52,53} Briefly, the tunable infrared spectrometer used for these studies was based on a 1 kHz regeneratively amplified Ti:sapphire laser system (800 nm, 100 fs, 900 μJ/pulse) and two optical parametric amplifiers (OPA). The signal and idler outputs of an IR OPA, pumped by 800 nm pulses, were difference-frequency mixed in an AgGaS₂ crystal to produce the tunable mid-IR probe pulses with a full width at half-maximum (fwhm) of ~120 cm⁻¹. Pump pulses were generated by a home-built visible noncollinear OPA (NOPA), whose broadband output was filtered by an interference filter (Optical Coating Laboratory Inc.) with ~10 nm bandwidth centered at 532 nm. The typical pulse energies of pump and probe pulses at the sample were ~10 nJ each, and their beam diameters at the sample were ~500 and 300 μm, respectively. After the sample, the probe was dispersed in a spectrometer and detected with a 32-element mercury cadmium telluride (MCT) array detector. The spectral resolution was 15 nm (~6 cm⁻¹ at 1900 cm⁻¹). Zero time delay and the instrument response function were determined with a Si wafer, which gave an instantaneous mid-IR absorption response after excitation at 532 nm. Typically, the instrument response function after the sample was well fit by a Gaussian function with 160 fs full width at half-maximum (fwhm). During the data collection, samples were constantly translated at a speed around 5 mm/min to avoid permanent photodamage.

Results

The X-ray diffraction (XRD) pattern of In₂O₃ nanoparticles is shown in Figure 1. The peak positions of the In₂O₃ sample agree well with the diffraction of bulk cubic In₂O₃ structure (Joint Committee on Powder Diffraction Standards (JCPDS) Card No. 71-2194), with strong peaks due to (222), (400), (440), and (622) planes, and are consistent with the results of previous studies of In₂O₃ nanoparticles prepared under similar conditions.⁵⁴ Shown in Figure 2 is a scanning electron microscopy (SEM) image of a typical film, which indicates a nanoporous network of nanoparticles with sizes ~10 nm in diameter.

The UV–vis absorption spectra of RuN3 and Ru505 in ethanol solution and on In₂O₃ films are shown in Figure 3. The

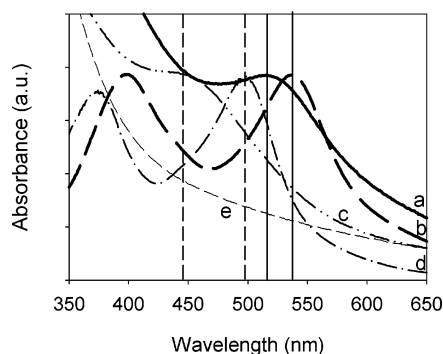


Figure 3. UV-vis absorption spectra of (a) RuN3 on In_2O_3 dry film (thick solid line), (b) RuN3 in ethanol solution (thick long-dashed line), (c) Ru505 on In_2O_3 dry film (dash-dot dotted line), (d) Ru505 in ethanol solution (dash-dotted line), and (e) unsensitized In_2O_3 (dashed line). Vertical solid lines show the lowest energy MLCT band position of RuN3 in ethanol solution and on In_2O_3 films, and the corresponding positions for Ru505 are indicated by two dashed lines.

lower energy metal-to-ligand charge-transfer (MLCT) band of RuN3 shifts from 537 nm in ethanol solution to 514 nm on dry In_2O_3 film (810 cm^{-1} shift). For Ru470, adsorption on In_2O_3 film leads to a blue shift from 482 nm in ethanol to 464 nm (805 cm^{-1} shift, spectra not shown). These blue shifts are similar to those previously observed on SnO_2 , which was attributed to the deprotonation of the $-\text{COOH}$ groups of ruthenium complexes on metal oxide semiconductor films and/or solvatochromic shifts from ethanol to air.⁴⁶ The peak position for the low-energy $^3\text{MLCT}$ band of Ru505 shifts from 492 nm in ethanol solution to 436 and 438 nm on dry In_2O_3 films and films in pH 2 buffer, respectively. These blue shifts ($\sim 2610\text{ cm}^{-1}$) are about 3 times larger than those of complexes without CN^- ligands and are attributed to specific interactions of the cyano group with the solvent molecules.^{55,56} In previous studies of related Ru-polypyridyl complexes, the solvatochromic shift was shown to increase with the number of CN^- ligands and correlate with the solvent acceptor number.^{55,56} It was suggested that donation of the electron pair from the N atoms of CN^- to acceptor orbitals of solvent molecules enhanced $d\pi(\text{Ru}^{\text{II}})-\pi^*(\text{CN})$ mixing, which stabilized the $d\pi(\text{Ru}^{\text{II}})$ orbital and increased the $d\pi(\text{Ru}^{\text{II}})-\pi^*(\text{bpy})$ MLCT transition energy.

Electron-transfer kinetics for RuN3, Ru505, and Ru470 sensitized dry In_2O_3 thin films measured at 532 nm excitation are shown in Figure 4. In this study, the pump wavelength at 532 nm was used to avoid excitation of the electron-hole pair in In_2O_3 , which has an indirect band gap at 2.62 eV (or 470 nm).⁴⁷ For clarity, the kinetics at different delay time windows are shown in panels a and b. These traces were obtained by averaging the absorbance change between 1880 and 1940 cm^{-1} , at which the signal contains negligible contribution from vibrational bands of Ru dyes and is dominated by electron absorption.^{45,46} In the same spectral window, a negligible electron absorption signal was observed in unsensitized films, as shown by the dashed lines in Figure 4, suggesting a negligible contribution of electrons generated by direct excitation of In_2O_3 to the observed signals in the sensitized films.

The kinetic traces shown in Figure 4 have been scaled by the absorption of dyes at 532 nm to correspond to the same number of absorbed photons, allowing a comparison of electron injection yields. The relative signal sizes of the three dyes on In_2O_3 films at 1 ns decrease from RuN3 to Ru505 to Ru470. For RuN3, the signal reaches a maximum value at ~ 100 ps and shows 10% decay within the 1 ns window. The decay may originate from either decrease of the electron absorption cross-section^{6,17} or back electron transfer.⁵³ The detailed decay

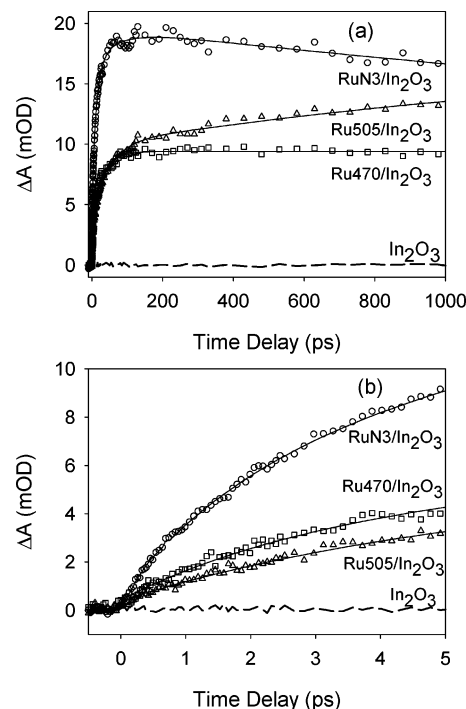


Figure 4. (a) Electron injection kinetics probed between 1880 and 1940 cm^{-1} for RuN3/ In_2O_3 (empty circle), Ru505/ In_2O_3 (empty triangle), and Ru470/ In_2O_3 (empty square) at dry conditions after 532 nm excitation. The size of the signal in different films has been scaled to correspond to the same number of absorbed photons. Negligible electron absorption signals are observed in unsensitized In_2O_3 films, as indicated by the dashed line at the bottom of the figure. The parameters for the multiexponential fits (solid lines) are listed in Table 1. Panel b shows the same kinetics at early time delays.

mechanism was not determined in this study due to the difficulty in obtaining vibrational spectra for RuN3 on In_2O_3 . Back electron transfer in the <1 ns window was observed previously in $\text{Re}(\text{Lp})(\text{CO})_3\text{Cl}$ ($\text{Lp} = 2,2'$ -bipyridine-4,4'- $\text{CH}_2-\text{PO}_3\text{H}_2$) sensitized SnO_2 . In that case, the CO stretching bands of the adsorbate in the ground and excited states and the oxidized form were monitored concurrently with the electron absorption signal.⁵³ Assuming that the maximum value observed for RuN3 on In_2O_3 corresponds to a 100% injection yield, the relative signal sizes correspond to injection yields of 67% and 48% at 1 ns for Ru505 and Ru470, respectively.

The rise of the electron absorption for all three Ru complexes on In_2O_3 is non-single-exponential. The kinetics for RuN3 can be fit by a three-exponential rise and a slow exponential decay ($\gg 1$ ns). For Ru 505 and 407, there are no noticeable decays in the <1 ns window, and the kinetics traces can be well fit by three-exponential rise functions. The fitting parameters are listed in Table 1. Since the signal sizes continue to grow beyond 1 ns, the time constant for the slowest component is not well determined by the fit. As a result, the amplitude-weighted average time constant, which depends sensitively on the slow component, is subject to large errors. Instead, we compare the half rise time $\tau_{1/2}$, the time when signal reaches 50% in these systems, which is also listed in Table 1.

Like many other metal oxides, the conduction band edge position of In_2O_3 is dependent on the concentration of adsorbed protons.⁴⁷ To study the sample at a well-determined band edge position, we measured the injection kinetics of the sensitized films submerged in a pH buffer. Because both sensitization and the electrode are stable under limited pH ranges, these experiments were only carried out at pH 2.^{47,57} The electron injection dynamics of RuN3, Ru505, and Ru470 on In_2O_3 at pH 2 are

TABLE 1: Parameters of a Multiexponential Fit to the Ru Dyes/In₂O₃^a

sensitizer	solvent	A ₁ (%), τ ₁ (ps)	A ₂ (%), τ ₂ (ps)	A ₃ (%), τ ₃ (ps)	τ _{1/2} (ps)	Y _{rel}
RuN3	dry	26, 2.0	57, 13	17, 64	5.1 ± 0.8	1
Ru505	dry	17, 4.6	33, 47	50, 2123	85 ± 20	0.67 ± 0.05
Ru470	dry	20, 3.2	26, 32	54, >1000	>200	0.48 ± 0.08
RuN3	pH 2	26, 1.4	46, 20	28, 69	5.9 ± 1.0	1
Ru505	pH 2	24, 5.0	33, 75	43, 5524	105 ± 20	0.65 ± 0.05
Ru470	pH 2	31, 3.0	36, 27	32, >1000	18 ± 5	0.68 ± 0.07

^a Amplitudes (A_i) and time constants (τ_i) for the multiexponential fits shown in Figures 4 and 5. τ_{1/2} is the time of 50% injection yield. Y_{rel} is the relative injection yield at 1 ns, which is assumed to be 1 for RuN3 under dry and pH 2 conditions. The error bars in τ_{1/2} and Y_{rel} are estimated from multiple measurements on different films.

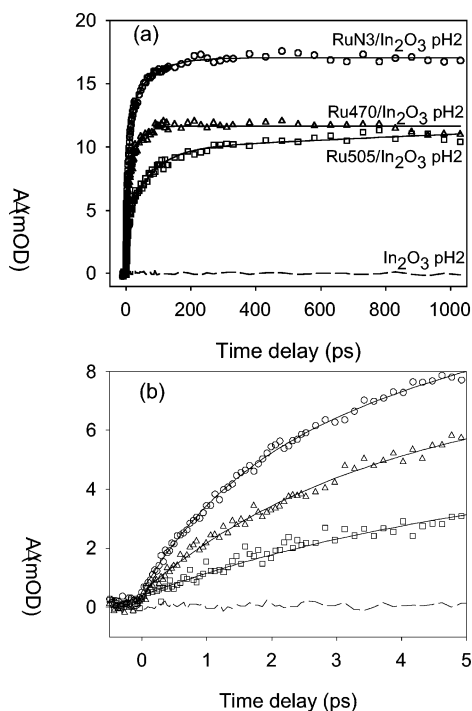


Figure 5. (a) Electron injection kinetics probed between 1880 and 1940 cm⁻¹ for RuN3 (empty circle), Ru505 (empty triangle), and Ru470 (empty square) sensitized In₂O₃ at a pH 2 buffer after 532 nm excitation. These signals have been scaled to correspond to the same number of absorbed photons. The solid lines are three-exponential fits to the data, whose parameters are listed in Table 1. The signal from unsensitized In₂O₃ signal at pH 2 is shown as a dashed line, which is negligible in comparison with the sensitized films. Panel b shows the same kinetics at early time delays.

shown in Figure 5. The signal sizes have been scaled to correspond to the same number of adsorbed photons. Again, the highest injection yield is observed for RuN3. Similar to the kinetics of Ru dyes on dry In₂O₃ films, the injection kinetics are non-single-exponential. Unlike RuN3 on dry In₂O₃ films, there are no noticeable decays of the signal at the <1 ns window. The kinetics traces can be well fit by three-exponential rise functions. The parameters for the three-exponential fits are listed in Table 1. Again, since injection is not completed at 1 ns for Ru505 and Ru470, the time constant for the slowest component is not well determined in this fit. To allow a quantitative comparison of injection rate, the injection yield of RuN3 is assumed to be 100% at 1 ns, from which the half rise times for the three systems are determined. Their values are also listed in Table 1.

To gain insight into its dependence on semiconductors, electron injection dynamics from RuN3 to In₂O₃, TiO₂, and SnO₂ at dry and pH 2 conditions are compared in Figures 6a and 6b, respectively. The data for RuN3/TiO₂ at pH 2 buffer was published in a previous paper and is not shown.¹⁷ All data were measured with 532 nm excitation, and all traces have been

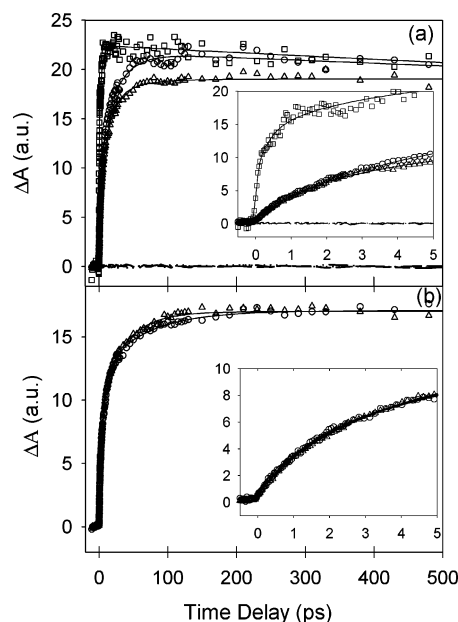


Figure 6. Comparison of normalized electron injection dynamics from RuN3 to In₂O₃ (circle), SnO₂ (triangle), and TiO₂ (square) nanocrystalline thin films (a) exposed to air and (b) submerged in pH 2 buffer. The injection kinetics for RuN3/TiO₂ in pH 2 has been published in ref 17 and is not shown here. All traces were normalized at 1 ns for clear comparison and were measured at 1880 and 1940 cm⁻¹ after 532 nm excitation. The kinetics traces in unsensitized In₂O₃, SnO₂, and TiO₂ films at dry conditions are displayed at the bottom of panel a, showing negligible electron absorption signals. The insets show the same data at early delay times.

normalized at 1 ns for better comparison. Electron injection kinetics to TiO₂ is clearly biphasic, dominated by a <100 fs injection component, while those to In₂O₃ and SnO₂ show negligible <100 fs injection components and are dominated by picosecond and longer components. Injection kinetics to In₂O₃ and SnO₂ are similar at both dry and pH 2. The time scales for injection and the reasons of the differences will be discussed in the next section.

Discussion

Effects of Energetics of Ru Dyes on the Injection Rate.

For electron injection from adsorbate excited state to the semiconductor, there exists a continuum of product states, each corresponding to the injected electron in one of the quasi-continuum k states. In the nonadiabatic limit, the total ET rate is the sum of the rates of these parallel pathways to different product states, giving rise to the dependence of ET rate on the density of states (DOS) in the semiconductor.^{61–64} Adopting an approach similar to Marcus and co-workers, the total forward electron-transfer rate may be expressed by the sum of the electron-transfer rate to all possible accepting states of the semiconductor.^{6,62–64}

$$k_{\text{ET}} = \frac{2\pi}{\hbar} \int_{-\infty}^{\infty} d\epsilon \rho(\epsilon) |\overline{H(\epsilon)}|^2 \frac{1}{\sqrt{4\pi\lambda k_{\text{B}}T}} \exp\left[-\frac{(\lambda + \Delta G_0 + \epsilon)^2}{4\lambda k_{\text{B}}T}\right] \quad (1)$$

where $\Delta G_0 = -e(E_{\text{CB}}^{\circ} - E^{\circ}(\text{S}^{+}/\text{S}^{*}))$ is the free energy change for electron transfer from the adsorbate excited state (with electrochemical potential $E^{\circ}(\text{S}^{+}/\text{S}^{*})$) to the conduction band edge (with electrochemical potential E_{CB}°); $\overline{H(\epsilon)}$ is the averaged electronic coupling between the adsorbate excited state and different k states in the semiconductor of the same energy ϵ ($=E - E_{\text{CB}}$, defined relative to the energy of the band edge); λ is the total reorganization energy, and $\rho(\epsilon)$ is the density of semiconductor states at energy ϵ .

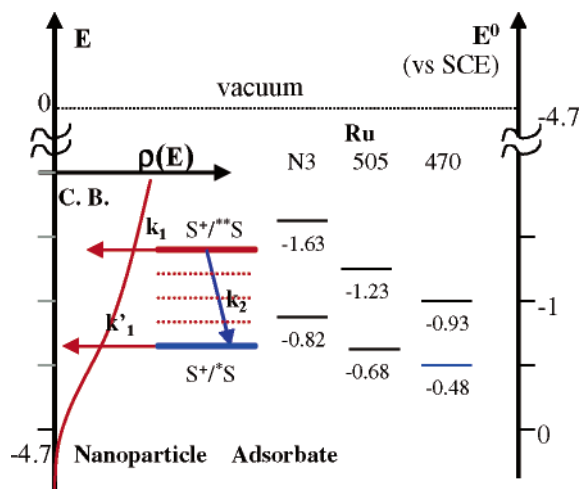
According to eq 1, the electron injection rate depends on the total available accepting states in the semiconductor as well as electronic coupling and reorganization energy. For a semiconductor, the density of conduction band states increases with the square root of energy for states near and above the conduction band edge, and the variation is more rapid below the band edge, where it is often modeled as an exponential tail for materials with large defect density.⁶⁵ This is expected to lead to a variation of ET rate with the relative position of the adsorbate potential with respect to the conduction band edge. For a larger $-\Delta G_0$, the density of accepting states in the conduction band of semiconductors increases, leading to a faster injection rate.⁶⁶

The expected trend was observed in a recent study of the pH dependence of electron injection rate from Re bipyridyl complexes to TiO_2 and SnO_2 .⁶⁶ It was shown that injection rate decreased with increasing pH value. From pH 0 to 9, the rate decreased by 3 orders of magnitude in TiO_2 , yet only slowed by a factor of ~ 4 in SnO_2 over a similar pH range. A comparison with predictions of nonadiabatic interfacial ET suggested that this dependence reflected the change of density of electron accepting states caused by the pH-dependent band edge position. When the pH increases, the band edge of metal oxides shifts to a more negative potential, and the density of electron accepting states decreases. On TiO_2 , the adsorbate excited-state oxidation potential is near the band edge; changes in band edge position lead to large variations of densities of accepting states. On SnO_2 , because of its ~ 0.5 V lower band edge position, the electron accepting states are further above the band edge, and their densities vary much slower with pH. These results suggest the dominating effect of density of electron accepting states on the rate of interfacial electron transfer.

As shown in Figure 4 and Table 1, the injection rates of Ru dyes on dry In_2O_3 film decrease from RuN3 to Ru505 and Ru470. While these complexes are similar in the two pairs of dcby ligands, they differ in the third pair of ligands, as shown in Chart 1. The excited-state oxidation potential (Scheme 1) decreases from RuN3 to Ru505 and Ru470, approaching the band edge of In_2O_3 . Assuming that the strength of electronic coupling to In_2O_3 is similar in these complexes, the electron injection rate of Ru dyes on In_2O_3 is expected to become slower from RuN3 to Ru505 to Ru470 due to less negative excited-state oxidation potential. Similar trends were also demonstrated for these dyes on dry TiO_2 ,¹⁷ Nb_2O_5 ,⁴⁵ and SnO_2 ⁴⁶ films.

For Ru N3 and Ru505 sensitized In_2O_3 films in pH 2 buffer, $\tau_{1/2}$ values for electron injection are similar to those on dry films. In pH 2 buffer, the conduction band edge is likely at a lower energy (or less negative electrochemical potential) than in dry films (due to the pH-dependent band edge), and there may be a higher solvent reorganization energy for ET. According to eq

SCHEME 1: Two-State Injection Model and Energetics for Electron Injection from Ru Complexes to Metal Oxides.^a



^a Left panel: A schematic representation of the two-state injection model. Electron injection (with rate constant k_1) from an unthermalized excited state ($^{**}\text{S}$, initially populated $^1\text{MLCT}$ state) competes with relaxation (rate constant k_2) to the bottom of the excited-state manifold $^*\text{S}$ (thermalized $^3\text{MLCT}$ state), from which injection can also occur (with rate constant k'_1). Right panel: The oxidation potentials (vs SCE) for the excited states ($^*\text{S}$ and $^{**}\text{S}$) of RuN3. The oxidation potentials are adopted from ref 17 and references therein. Values of $\text{S}^{+}/^*\text{S}$ are calculated from ground-state potential and emission energy, and values of $\text{S}^{+}/^{**}\text{S}$ are calculated from ground-state potential and the energy of the excitation photon at 532 nm.

1, a lower conduction band edge should lead to a faster ET rate, and an increase in reorganization energy should slow the rate. The similar ET rates in dry film and pH 2 buffer for RuN3 and Ru505 may be due to the partial cancellation of these changes. For Ru470, $\tau_{1/2}$ has increased significantly in pH 2 buffer and has become shorter than that of Ru505, deviating from the trend expected from energetics consideration alone. Although the reasons for deviation remain unclear, it was also observed for these complexes on SnO_2 films in pH 2 buffer.

Comparison of Injection Dynamics from RuN3 to In_2O_3 , TiO_2 , and SnO_2 . Many previous studies have shown that the injection dynamics from RuN3 to TiO_2 are distinctly biphasic, consisting of a <100 fs ultrafast component and multiexponential slower components on a picosecond or longer time scale.^{13–27} The amplitude of the <100 fs component was shown to depend on the excitation wavelength, suggesting that it occurs from unthermalized excited states.^{17,24–26} Our previous study showed that for RuN3/ TiO_2 at pH 2, the yield of injection from the unthermalized excited state changed from $\sim 63\%$ at 400 nm excitation to $\sim 44\%$ at 530 nm excitation.¹⁷ The slow injection components have been attributed to injection from the relaxed triplet excited state near the conduction band edge. It is believed that the slower injection rate from the relaxed state results from a reduced density of accepting states at the band edge¹⁷ and from intraligand charge-transfer dynamics.²¹

More recently, electron injection dynamics from RuN3 to SnO_2 have also been reported, showing a noticeably smaller <100 fs injection component than that to TiO_2 .^{23,46} We have previously proposed a two-state injection model to account for the biphasic injection kinetics and its excitation wavelength dependence, as shown in Scheme 1.¹⁷ According to this model, injection from the unthermalized excited state (with rate constant k_1) competes with the relaxation to the lower excited state (with rate constant k_2). As a result of this competition, the amplitude

TABLE 2: Comparison of Electron Injection Kinetics from RuN3 to In₂O₃, SnO₂, and TiO₂^a

semiconductors	condition	$A_{(<100\text{ fs})}^c$	$\tau_{1/2}$ (ps)	m^*/m_e^b
TiO ₂	dry	~60	<0.1	5–10
In ₂ O ₃	dry	~0	5.1 ± 0.8	0.3
SnO ₂	dry	~0	4.9 ± 0.5	0.3
TiO ₂	pH2	~58 ^d	<0.1	
In ₂ O ₃	pH2	~0	5.9 ± 1.0	
SnO ₂	pH2	~0	5.9 ± 0.5	

^a All data are taken with 532 nm excitation. ^b m^* is the effective mass of the conduction band electron; m_e is the rest mass of free electrons.^{58–60} ^c $A_{(<100\text{ fs})}$ is apparent amplitude (in percentage) of the <100 fs injection component before correcting for cross-section decay.¹⁷

^d Adapted from ref 17. The error bars in $\tau_{1/2}$ are estimated from multiple measurements on different films.

of the fast component is determined by $k_1/(k_1 + k_2)$. A smaller amplitude of the <100 fs component in RuN3 sensitized SnO₂ suggests a slower ET rate from the unthermalized state (k_1) to SnO₂ than that to TiO₂.⁴⁶

As shown in Figures 6a and 6b, the injection kinetics traces in RuN3 sensitized In₂O₃ and SnO₂ films measured after 532 nm excitation show no noticeable <100 fs injection components. In a previous study of RuN3 on SnO₂, we reported that the injection kinetics measured at 400 nm excitation contains a small (~8%) but noticeable fast component. We have also shown for both RuN3 on TiO₂¹⁷ and ZnO⁴³ that the amplitude of the fast component decreases at lower excitation energy. The negligible amplitude of the fast component for RuN3/SnO₂ at 532 nm excitation is consistent with the previously observed wavelength dependence and provides further evidence that it occurs from the unthermalized excited states. This is dramatically different from RuN3/TiO₂ in dry films (shown in Figure 6a) and at pH 2 buffer (reported previously¹⁷). The injection kinetics traces measured at 532 nm excitation show a significant <100 fs injection component with apparent amplitudes of ~60%.

The above comparisons suggest that the injection rate from the unthermalized excited states for RuN3 on In₂O₃ is similar to that on SnO₂ and is much smaller than that on TiO₂. This is consistent with the trend observed in a recent series of experiments that compared electron injection dynamics from Ru polypyridyl dyes to TiO₂,^{6,17} ZnO,^{43,44} Nb₂O₅,⁴⁵ and SnO₂.⁴⁶ It was shown that the amplitude of the fast component followed this order: TiO₂ > Nb₂O₅ >> SnO₂ ≈ ZnO,^{45,46} suggesting faster injection rates from the unthermalized excited state to TiO₂ and Nb₂O₅ than those to SnO₂ and ZnO. As indicated in eq 1, in the nonadiabatic limit, the electron injection rate is proportional to the density of accepting states in the semiconductor conduction band. The conduction band density of states can be estimated from its electron effective mass, m^* ⁶⁵

$$\rho_0(\epsilon) d\epsilon = \frac{(2m^*)^{3/2}}{2\pi^2\hbar^3} \sqrt{\epsilon} d\epsilon \quad (2)$$

As listed in Table 2, the electron effective mass in d-type conduction bands (~5–10 m_e for TiO₂ and 3 m_e Nb₂O₅) is usually orders of magnitude higher than sp-type conduction bands (~0.3 m_e for SnO₂ and ZnO).⁶⁵ Therefore, at energy levels significantly above the band edge, the density of states in sp conduction bands is orders of magnitude smaller than that in d-type conduction bands. We speculated that this difference was the main reason for the much slower injection rate to SnO₂ and ZnO. Similar to SnO₂ and ZnO, the conduction band of In₂O₃ is comprised primarily of empty s and p orbitals of In³⁺ and has an electron effective mass of 0.3 m_e .⁶⁰ The lack of fast

component amplitude in the injection kinetics from RuN3 to In₂O₃ further supports the above hypothesis.

For RuN3 on SnO₂ and In₂O₃ at 532 nm excitation, the lack of a <100 fs component suggests that injection proceeds from the relaxed ³MLCT states, which are ~0.8 V above the band edge. In light of similar conduction band edge positions and electron effective masses in In₂O₃ and SnO₂,^{3,49} one would expect similar electron injection rates if the electronic coupling strengths with RuN3 are similar in these systems. Indeed, half times for injection are very similar in these systems as shown in Table 2 and Figures 6a and 6b. In the case of TiO₂, because of the ~0.5 V higher band edge position, injection likely occurs to states near or below the band edge, which may contain significant contributions from defect states. For this reason, we have not attempted to compare the slow injection components in RuN3 sensitized TiO₂ with the kinetics in SnO₂ and ZnO.

Summary

Electron injection dynamics from Ru polypyridyl complexes to In₂O₃ nanocrystalline thin films were investigated by monitoring the mid-IR absorption signal of injected electrons in a semiconductor. The injection kinetics were found to be non-single-exponential with a negligible <100 fs injection component. In dry films, the injection rates were found to decrease in the order of RuN3 > Ru470 > Ru505, following the lowering of excited-state potentials in these complexes. In pH 2 buffer, the injection rates from RuN3 and Ru505 remained similar to those in dry films but increased significantly for Ru470.

The injection kinetics from RuN3 to different semiconductors were also compared to understand their dependence on the nature of semiconductors. The injection kinetics on In₂O₃ was similar to that on SnO₂ but dramatically different from that on TiO₂. A significant ultrafast (<100 fs) injection component was observed on TiO₂ but not on SnO₂ and In₂O₃. It suggested a much faster rate of injection from unthermalized excited states to TiO₂ than to SnO₂ and In₂O₃. The similar injection kinetics in In₂O₃ and SnO₂ were attributed to similar conduction band edge position and density of states in these materials. Their difference from TiO₂ was attributed to the ~200-fold smaller density of states in the sp-type (SnO₂, and In₂O₃) than in d-type (TiO₂) conduction bands.

Acknowledgment. Financial support was provided by the Division of Chemical Sciences, Office of Basic Energy Research, U. S. Department of Energy. This work is also supported in part by the donors of the Petroleum Research Fund and the Emory University Research Committee. We are grateful to Dr. Robert P. Apkarian, the director of the Integrated Microscopy and Microanalytical Facility, and JEOL for the HRSEM measurement. T.L. is an Alfred P. Sloan fellow.

References and Notes

- (1) Miller, R. J. D.; McLendon, G. L.; Nozik, A. J.; Schmickler, W.; Willig, F. *Surface Electron-Transfer Processes*; VCH Publishers: New York, 1995.
- (2) Kamat, P. V. *Chem. Rev.* **1993**, 93, 267.
- (3) Hagfeldt, A.; Gratzel, M. *Chem. Rev.* **1995**, 95, 49.
- (4) Michael Graetzel Festschrift. *Coord. Chem. Rev.* **2004**, 248, 1161–1530.
- (5) Anderson, N. A.; Lian, T. *Annu. Rev. Phys. Chem.* **2005**, 56, 491.
- (6) Asbury, J. B.; Hao, E.; Wang, Y.; Ghosh, H. N.; Lian, T. *J. Phys. Chem. B* **2001**, 105, 4545.
- (7) Watson, D., F.; Meyer, G., J. *Annu. Rev. Phys. Chem.* **2005**, 56, 119.
- (8) Nozik, A. J.; Memming, R. *J. Phys. Chem.* **1996**, 100, 13061.
- (9) Lewis, N. S. *J. Phys. Chem. B* **1998**, 102, 4843.

- (10) Nazeeruddin, M. K.; Kay, A.; Rodicio, I.; Humphrybaker, R.; Muller, E.; Liska, P.; Vlachopoulos, N.; Gratzel, M. *J. Am. Chem. Soc.* **1993**, *115*, 6382.
- (11) O'Regan, B.; Gratzel, M. *Nature* **1991**, *353*, 737.
- (12) Bach, U.; Lupo, D.; Comte, P.; Moser, J. E.; Weissortel, F.; Salbeck, J.; Spreitzer, H.; Gratzel, M. *Nature* **1998**, *395*, 583.
- (13) Tachibana, Y.; Nazeeruddin, M. K.; Gratzel, M.; Klug, D. R.; Durrant, J. R. *Chem. Phys.* **2002**, *285*, 127.
- (14) Tachibana, Y.; Haque, S. A.; Mercer, I. P.; Moser, J. E.; Klug, D. R.; Durrant, J. R. *J. Phys. Chem. B* **2001**, *105*, 7424.
- (15) Durrant, J. R.; Tachibana, Y.; Mercer, I.; Moser, J. E.; Gratzel, M.; Klug, D. R. *Z. Phys. Chem.* **1999**, *212*, 93.
- (16) Tachibana, Y.; Moser, J. E.; Graetzel, M.; Klug, D. R.; Durrant, J. R. *J. Phys. Chem.* **1996**, *100*, 20056.
- (17) Asbury, J. B.; Anderson, N. A.; Hao, E.; Lian, T. *J. Phys. Chem. B* **2003**, *107*, 7376.
- (18) Asbury, J. B.; Ellingson, R. J.; Ghosh, H. N.; Ferrere, S.; Nozik, A. J.; Lian, T. *J. Phys. Chem. B* **1999**, *103*, 3110.
- (19) Ellingson, R. J.; Asbury, J. B.; Ferrere, S.; Ghosh, H. N.; Sprague, J. R.; Lian, T.; Nozik, A. J. *J. Phys. Chem. B* **1998**, *102*, 6455.
- (20) Hannappel, T.; Burfeindt, B.; Storck, W.; Willig, F. *J. Phys. Chem. B* **1997**, *101*, 6799.
- (21) Benko, G.; Kallioinen, J.; Myllyperkio, P.; Trif, F.; Korppi-Tommola, J. E. I.; Yartsev, A. P.; Sundstrom, V. *J. Phys. Chem. B* **2004**, *108*, 2862.
- (22) Kallioinen, J.; Benko, G.; Myllyperkio, P.; Khriachtchev, L.; Skarman, B.; Wallenberg, R.; Tuomikoski, M.; Korppi-Tommola, J. E. I.; Sundstrom, V.; Yartsev, A. P. *J. Phys. Chem. B* **2004**, *108*, 6365.
- (23) Benko, G.; Myllyperkio, P.; Pan, J.; Yartsev, A. P.; Sundstrom, V. *J. Am. Chem. Soc.* **2003**, *125*, 1118.
- (24) Kallioinen, J.; Benko, G.; Sundstrom, V.; Korppi-Tommola, J. E. I.; Yartsev, A. P. *J. Phys. Chem. B* **2002**, *106*, 4396.
- (25) Benko, G.; Kallioinen, J.; Korppi-Tommola, J. E. I.; Yartsev, A. P.; Sundstrom, V. *J. Am. Chem. Soc.* **2002**, *124*, 489.
- (26) Kuciauskas, D.; Monat, J. E.; Villahermosa, R.; Gray, H. B.; Lewis, N. S.; McCusker, J. K. *J. Phys. Chem. B* **2002**, *106*, 9347.
- (27) Heimer, T. A.; Heilweil, E. J. *J. Phys. Chem. B* **1997**, *101*, 10990.
- (28) Haque, S. A.; Tachibana, Y.; Willis, R. L.; Moser, J. E.; Graetzel, M.; Klug, D. R.; Durrant, J. R. *J. Phys. Chem. B* **2000**, *104*, 538.
- (29) Haque, S. A.; Tachibana, Y.; Klug, D. R.; Durrant, J. R. *J. Phys. Chem. B* **1998**, *102*, 1745.
- (30) Heimer, T. A.; Heilweil, E. J.; Bignozzi, C. A.; Meyer, G. J. *J. Phys. Chem. A* **2000**, *104*, 4256.
- (31) Hasselmann, G. M.; Meyer, G. J. *J. Phys. Chem. B* **1999**, *103*, 7671.
- (32) Kuciauskas, D.; Freund, M. S.; Gray, H. B.; Winkler, J. R.; Lewis, N. S. *J. Phys. Chem. B* **2001**, *105*, 392.
- (33) Hara, K.; Horiguchi, T.; Kinoshita, T.; Sayama, K.; Sugihara, H.; Arakawa, H. *Sol. Energy Mater. Sol. Cells* **2000**, *64*, 115.
- (34) Sayama, K.; Sugihara, H.; Arakawa, H. *Chem. Mater.* **1998**, *10*, 3825.
- (35) Rensmo, H.; Keis, K.; Lindstrom, H.; Sodergren, S.; Solbrand, A.; Hagfeldt, A.; Lindquist, S. E.; Wang, L. N.; Muhammed, M. *J. Phys. Chem. B* **1997**, *101*, 2598.
- (36) Aegerter, M. A. *Sol. Energy Mater. Sol. Cells* **2001**, *68*, 401.
- (37) Aegerter, M. A.; Schmitt, M.; Guo, Y. *Int. J. Photoenergy* **2002**, *4*, 1.
- (38) Hu, L. L.; Wolf, M.; Gratzel, M.; Jiang, Z. H. *J. Sol-Gel Sci. Technol.* **1995**, *5*, 219.
- (39) Barros Filho, D. d. A.; Abreu Filho, P. P.; Werner, U.; Aegerter, M. A. *J. Sol-Gel Sci. Technol.* **1997**, *8*, 735.
- (40) Lenzmann, F.; Krueger, J.; Burnside, S.; Brooks, K.; Graetzel, M.; Gal, D.; Ruehle, S.; Cahen, D. *J. Phys. Chem. B* **2001**, *105*, 6347.
- (41) Bedja, I.; Hotchandani, S.; Kamat, P. V. *J. Phys. Chem.* **1994**, *98*, 4133.
- (42) Ferrere, S.; Zaban, A.; Gregg, B. A. *J. Phys. Chem. B* **1997**, *101*, 4490.
- (43) Anderson, N. A.; Ai, X.; Lian, T. *J. Phys. Chem. B* **2003**, *107*, 14414.
- (44) Asbury, J. B.; Wang, Y.; Lian, T. *J. Phys. Chem. B* **1999**, *103*, 6643.
- (45) Ai, X.; Guo, J.; Anderson, N. A.; Lian, T. *J. Phys. Chem. B* **2004**, *108*, 12795.
- (46) Ai, X.; Anderson, N. A.; Guo, J.; Lian, T. *J. Phys. Chem. B* **2005**, *109*, 7088.
- (47) *Semiconductor Electrodes*; Finklea, H. O., Ed.; Studies in Physical and Theoretical Chemistry 55; Elsevier: New York, 1988.
- (48) Anderson, S.; Constable, E. C.; Dare-Edwards, M. P.; Goodenough, J. B.; Hamnett, A.; Seddon, K. R.; Wright, R. D. *Nature* **1979**, *280*, 571.
- (49) Erbs, W.; Kiwi, J.; Gratzel, M. *Chem. Phys. Lett.* **1984**, *110*, 648.
- (50) Poznyak, S. K.; Golubev, A. N.; Kulak, A. I. *Surf. Sci.* **2000**, *454*–456, 396.
- (51) Poznyak, S. K.; Kulak, A. I. *Electrochim. Acta* **2000**, *45*, 1595.
- (52) Anderson, N. A.; Ai, X.; Chen, D.; Mohler, D. L.; Lian, T. *J. Phys. Chem. B* **2003**, *107*, 14231.
- (53) Guo, J.; She, C.; Lian, T. *J. Phys. Chem. B* **2005**, *109*, 7095.
- (54) Chen, X.; Zhang, Z.; Zhang, X.; Liu, J.; Qian, Y. *Chem. Phys. Lett.* **2005**, *407*, 482.
- (55) Timpson, C. J.; Bignozzi, C. A.; Sullivan, B. P.; Kober, E. M.; Meyer, T. J. *J. Phys. Chem.* **1996**, *100*, 2915.
- (56) Chen, P. Y.; Meyer, T. J. *Chem. Rev.* **1998**, *98*, 1439.
- (57) Tahar, R. B. H.; Takayuki, B.; Ohya, Y.; Takahashi, Y. *J. Appl. Phys.* **1997**, *82*, 865.
- (58) Redmond, G.; Fitzmaurice, D.; Graetzel, M. *J. Phys. Chem.* **1993**, *97*, 6951.
- (59) Enright, B.; Fitzmaurice, D. *J. Phys. Chem.* **1996**, *100*, 1027.
- (60) Fujiwara, H.; Kondo, M. *Phys. Rev. B* **2005**, *71*, 0751091.
- (61) Marcus, R. A. *J. Chem. Phys.* **1965**, *43*, 679.
- (62) Gao, Y. Q.; Georgievskii, Y.; Marcus, R. A. *J. Chem. Phys.* **2000**, *112*, 3358.
- (63) Gao, Y. Q.; Marcus, R. A. *J. Chem. Phys.* **2000**, *113*, 6351.
- (64) Gosavi, S.; Marcus, R. A. *J. Phys. Chem. B* **2000**, *104*, 2067.
- (65) Pankove, J. I. *Optical Processes in Semiconductors*; Dover: New York, 1975.
- (66) She, C.; Anderson, N. A.; Guo, J.; Liu, F.; Goh, W.; Chen, D.-T.; Mohler, D. L.; Tian, Z.-Q.; Hupp, J.; Lian, T. *J. Phys. Chem. B* **2005**, *109*, 19345.